Global modelling of tungsten impurity transport based on the drift-kinetic equation, Nuclear Fusion

Global modelling of tungsten impurity transport based on drift-kinetic equation

Ryutaro Kanno[1,2], Gakushi Kawamura[1,2], Masanori Nunami[1,2], Yuki Homma[3], Akiyoshi Hatayama[4], and Kazuo Hoshino[4]

[1] National Institute for Fusion Science, National Institutes of Natural Sciences, Toki 509-5292, Japan

[2] Department of Fusion Science, The Graduate University for Advanced Studies, SOKENDAI, Toki 509-5292, Japan

[3] Rokkasho Fusion Institute, National Institutes for Quantum and Radiological Science and Technology, Rokkasho 039-3212, Japan

[4] Graduate School of Science and Technology, Keio University, Yokohama 223-8522, Japan

E-mail: kanno@nifs.ac.jp

Revised: 25 October 2019

Abstract. A global kinetic simulation model of collisional impurity transport is developed for evaluating the radial particle flux of tungsten impurity in the edge region of a tokamak plasma. Here, the plasma including the impurity and the background ion is presupposed to be quasi-steady. The simulation model is based on the drift-kinetic equation of the impurity affected by the friction force and the thermal force, which were formulated in the previous study [Homma Y. *et al* 2016 *Nucl. Fusion* **56** 036009]. The model is implemented in a drift-kinetic δf simulation code. We find that the magnetic drift term in the drift-kinetic equation causes the "global effect" on the impurity transport. Here, the global effect means that the solution δf_Z of the drift-kinetic equation (and also the radial particle flux) on a magnetic flux surface is influenced by the values of the solution δf_Z all over the edge region.

Keywords: tungsten impurity, collisional transport, drift-kinetic modelling

Submitted to: *Nucl. Fusion*

1. Introduction

When the plasma facing components of fusion reactors are made of tungsten (W), the accumulation of W impurity in the core of the toroidal plasma is one of the most critical issues for operating the fusion reactors due to their excessive radiative cooling. Therefore, understanding of the impurity transport process from the divertor region towards the core and assessment of the accumulation level in the core are very important. In order to predict the impurity accumulation precisely, it is necessary to develop appropriate theoretical and numerical models for simulating the transport process. In the present paper, we will discuss collisional transport, in particular, neoclassical transport of W impurity for evaluating the radial particle flux of the W impurity in the edge region of a tokamak plasma. In collisional transport phenomena in the edge region, multiple time scales of Coulomb collisions between plasma particles often appear [1]. For the modelling of the collisional impurity transport, one of the most difficult problems is how to handle excessive differences among the multiple time scales because the transport simulation becomes time-consuming. Here, the plasma including the W impurity and the background ion is presupposed to be quasi-steady.

For mitigating the cooling, the number density n_Z of the W impurity is required to be 10^4-10^5 or more times smaller than the number density n_i of the background ion in the edge region [2, 3]. When the radial particle flux of the W impurity is estimated in this situation, the Coulomb collisions have multiple time scales. Suppose, for instance, that the number densities and the temperatures of the background ion and the W impurity are $n_i \sim 3\times10^{19}$ m^{-3}, $n_Z \sim 1\times10^{15}$ m^{-3}, and $T_i \sim T_Z \sim 100$ eV, then the characteristic time scales are given as the deflection time between the W impurity and the background ion $\tau_{\rm D}^{Zi} \sim 8\times10^{-6}$ s, the deflection time between the W impurities $\tau_{\rm D}^{ZZ} \sim 4\times10^{-2}$ s, the slowing down time $\tau_{\rm s} \sim 9\times10^{-2}$ s, etc. Here, the charge number of the W impurity is assumed as $Z = +4$ under low electron temperature compared to T_i, and the background ion is set to deuteron (D^+). It should be noted that these characteristic time scales depend on the value of Z as shown below in equations (7), (10), and (13).

Such an excessive difference among the characteristic time scales causes the difficulty in executing a kinetic simulation of the collisional impurity transport. It is not practical to execute the kinetic simulation treating time evolution of all the species of plasma particles, which consist of W impurities having various charge numbers, background ions, electrons, and the others. Hence, the equations to be solved for investigating collisional transport properties of the W impurity having a charge number Z should be simplified. In this paper, a drift-kinetic simulation model is developed for evaluating the radial particle flux of the W impurity, which is caused by Coulomb collisions, in the edge region of a tokamak plasma.

The simulation model is constructed as follows. First, it is natural that the Coulomb collision between the W impurity and the electron is ignored in the evaluation of the radial particle flux because of the excessive small mass ratio of the electron to the W impurity. On the other hand, as treated in previous studies [4, 5, 6, 7], the

Coulomb collision between the W impurity and the background ion is considered in the evaluation. Conversely, effects of the Coulomb collision between the background ion and the W impurity on the distribution function f_i of the background ion are ignored by taking account of the fact that n_Z is 10^4-10^5 times smaller than n_i. In this case, the distribution function f_i is determined independently of the distribution function f_Z of the W impurity, and f_i is assumed to be represented by using the 13-moments approximation [5]. Here, the collisionality of the background ion in the edge region is assumed to be in the Pfirsch-Schlüter (PS) regime. Referring to the previous studies, in the present paper the Coulomb collision between the W impurity and the background ion and the self-collision of the W impurity are taken into consideration in the drift-kinetic equation of the W impurity. Here, the Coulomb collisions between W impurities having various charge numbers are usually ignored under the trace impurity approximation [5, 6, 7, 8, 9]. In order to check the influence of disregarding these Coulomb collisions, the self-collision of the W impurity having a charge number Z is purposely left in the present simulation model. As shown below, the validity of ignoring the self-collision is confirmed in the evaluation of the radial particle flux.

From the previous studies, it is known that the Coulomb collision between the W impurity and the background ion is interpreted as the friction force and the thermal force acting on the impurity particles along magnetic field lines. In the previous studies [5, 6], a full-orbit particle simulation of the collisional impurity transport was performed for evaluating the radial particle flux of the W impurity across a magnetic flux surface in the edge region in a circular tokamak field. In the full-orbit particle simulation, full-orbits of the W impurity particles, which include their gyro-motions and start from the initial positions distributed uniformly on the magnetic flux surface, are traced under considering only the binary Coulomb collision between the W impurity and the background ion. Here, the distribution function of the background ion is set by using the 13-moments approximation, which is the same as equation (3) shown below, and the distribution function of the W impurity evolves with time from the Maxwellian function. It is shown that the radial particle flux evaluated in the full-orbit particle simulation is basically consistent with the theoretical estimate obtained under considering two neoclassical effects, i.e., the neoclassical inward pinch and the neoclassical temperature screening effect [6, 10]. These neoclassical effects originate from the friction force and the thermal force on the W impurity particles in the parallel directions. Here, the friction and the thermal forces are formulated in [6].

On the other hand, we should note that the global effect, which originates from finite orbit widths of the W impurity guiding centres across the neighbouring magnetic flux surfaces, is ignored in the theoretical estimate. The orbit width of a W impurity guiding centre is estimated as $\lesssim 1$ cm. The finite orbit widths in tokamak plasmas do not usually cause unignorable differences from the conventional neoclassical estimates, as is also shown in appendix. When considering the friction and the thermal forces, the global effect caused by the finite orbit widths appears after the relaxation time of the parallel flow velocity of the W impurity, as seen below. Here, the parallel flow velocity

is directly related to the strength of the friction force. The relaxation is characterised by the slowing down time, and the relaxation time is ten or more times longer than the slowing down time if the time evolution of f_Z starts from the Maxwellian function. This point has not been sufficiently taken into account in the previous studies. Therefore, in this paper we investigate how strongly the global effect impacts on the radial particle flux of the W impurity, by developing the solver of the drift-kinetic equation.

Here, the global effect is caused by the magnetic drift term in the left-hand side of the drift-kinetic equation. This term is taken into consideration in a global code in general, for example, PERFECT [11], XGC0 [12], etc. For example, in PERFECT code, the linearised Fokker-Planck (FP) operator is used for representing Coulomb collisions. In general, a simulation of the relaxation of the parallel flow velocity is highly time-consuming in the case of employing the linearised FP operator. In this paper, in order to reduce the calculation cost of the transport simulation on the slowing down time scale, the simple formula of the friction force and the thermal force, which is mentioned below in equation (5), is employed for treating the Coulomb collision between the W impurity and the background ion.

For explaining the global modelling of the impurity transport on the slowing down time scale and showing the simulation results affected by the global effect, this paper is organised as follows. In section 2, the global modelling based on the drift-kinetic equation of the W impurity is shown, and the model is implemented in the drift-kinetic δf simulation code, KEATS [13, 14]. The global effect on the radial particle flux is examined in benchmarks of the simulation code. The summary and discussions are given in section 3. In appendix, the difference between the local and the global modelling is explained in detail. Here, the theoretical estimate is reproduced by the local model.

2. Transport modelling based on drift-kinetic equation

2.1. Global simulation model

Both of the distribution functions of the W impurity and the background ion, f_Z and f_i, are assumed to be quasi-steady. The drift-kinetic equation of the W impurity is given as

$$\left\{ \frac{\partial}{\partial t} + \left(\mathbf{v}_\parallel + \mathbf{v}_\mathrm{d} \right) \cdot \frac{\partial}{\partial \mathbf{x}} + \dot{v}_\parallel \frac{\partial}{\partial v_\parallel} \right\} f_Z = C(f_Z, f_i) + C(f_Z, f_Z) + S, \tag{1}$$

where $\dot{v} = 0$, $\dot{v}_\parallel = -\{\mathbf{B}^* \cdot (\mu/m_Z)\nabla B\}/B^*_\parallel$ [15, 16], $C(f_Z, f_i)$ is the Coulomb collision term between the W impurity and the background ion D^+, $C(f_Z, f_Z)$ is the self-collision term of the W impurity, and S is the source/sink term. The parallel and drift velocities are given as $\mathbf{v}_\parallel = v_\parallel \mathbf{B}^*/B^*_\parallel$ and $\mathbf{v}_\mathrm{d} = \{(\mu/Ze)\mathbf{b} \times \nabla B\}/B^*_\parallel$ [15, 16]. The magnetic moment μ is represented as $\mu = m_Z {v_\perp}^2/2B$, $v_\perp = \sqrt{v^2 - {v_\parallel}^2}$, $\mathbf{B}^* = \mathbf{B} + (m_Z v_\parallel/Ze)\nabla \times \mathbf{b}$, $B^*_\parallel = \mathbf{b} \cdot \mathbf{B}^*$, $\mathbf{b} = \mathbf{B}/B$ is the unit vector of magnetic field $\mathbf{B}$, $B = |\mathbf{B}|$, e is the elementary charge, and the W mass is written by m_Z. The electric field $\mathbf{E}$ is ignored and is set to $\mathbf{E} = 0$.

When both f_Z and f_i are quasi-steady, these distribution functions are close to Maxwellian functions. Here, the Maxwellian functions of the impurity and the background ion are given as $f_{\mathrm{M},Z}$ and $f_{\mathrm{M},i}$, respectively. Decomposing the distribution functions f_Z and f_i to $f_Z = f_{\mathrm{M},Z} + \delta f_Z$ and $f_i = f_{\mathrm{M},i} + \delta f_i$, the impurity-ion collision term $C(f_Z, f_i)$ is expressed as

$$\begin{aligned} C(f_Z, f_i) &= C(f_{\mathrm{M},Z}, f_{\mathrm{M},i}) + C(f_{\mathrm{M},Z}, \delta f_i) + C(\delta f_Z, f_{\mathrm{M},i}) + C(\delta f_Z, \delta f_i) \\ &\approx C(f_{\mathrm{M},Z}, \delta f_i) + C(\delta f_Z, f_{\mathrm{M},i}). \end{aligned} \tag{2}$$

The first term $C(f_{\mathrm{M},Z}, f_{\mathrm{M},i})$ is zero when the temperature of the impurity is the same as the temperature of the background ion. Hereafter, $C(f_{\mathrm{M},Z}, f_{\mathrm{M},i}) = 0$. The fourth term $C(\delta f_Z, \delta f_i)$ is ignored because this term is negligibly small compared to the other terms. When the background ion is highly collisional, the distribution function f_i is given by using the PS flow velocity $\mathbf{V}_{i,\parallel}^{\mathrm{PS}} = V_{i,\parallel}^{\mathrm{PS}}\mathbf{b}$ and the PS heat flux $\mathbf{q}_{i,\parallel}^{\mathrm{PS}} = q_{i,\parallel}^{\mathrm{PS}}\mathbf{b}$ in the 13-moments approximation [5]. Here, the 13-moments approximation of f_i is expressed as [17]

$$f_i(\mathbf{x}, \mathbf{v}) \approx n_i \left(\frac{1}{\pi {v_{\mathrm{th},i}}^2}\right)^{3/2} \exp\left\{-\frac{\mathbf{w}^2}{{v_{\mathrm{th},i}}^2}\right\} \left[1 - \left(1 - \frac{2\,\mathbf{w}^2}{5\,{v_{\mathrm{th},i}}^2}\right) \frac{2\,\mathbf{q}_{i,\parallel}^{\mathrm{PS}} \cdot \mathbf{w}}{T_i n_i {v_{\mathrm{th},i}}^2}\right], \tag{3}$$

where $\mathbf{w} = \mathbf{v} - \mathbf{V}_{i,\parallel}^{\mathrm{PS}}$, m_i is the ion mass, and $v_{\mathrm{th},i} = \sqrt{2T_i/m_i}$ is the thermal speed of the background ion. Under the conditions of $|V_{i,\parallel}^{\mathrm{PS}}/v_{\mathrm{th},i}| \ll 1$ and $|q_{i,\parallel}^{\mathrm{PS}}/T_i n_i v_{\mathrm{th},i}| \ll 1$, the distribution function f_i is decomposed as

$$f_i(\mathbf{x}, \mathbf{v}) \approx f_{\mathrm{M},i} + \delta f_i(\mathbf{x}, \mathbf{v}; \mathbf{V}_{i,\parallel}^{\mathrm{PS}}, \mathbf{q}_{i,\parallel}^{\mathrm{PS}}). \tag{4}$$

As shown in [6], using equation (4), the Coulomb collisional force $\mathbf{R}_{Zi,\parallel} = R_{Zi,\parallel}\mathbf{b}$, which consists of the friction force and the thermal force acting on the impurity particles along magnetic field lines, is approximately given as

$$\mathbf{R}_{Zi,\parallel} \approx -C_1 \frac{n_i m_i}{\tau_{\mathrm{s}}} \left(\mathbf{V}_{Z,\parallel} - \mathbf{V}_{i,\parallel}^{\mathrm{PS}}\right) + \mathbf{R}_{\mathrm{th},\parallel}, \tag{5}$$

where $\mathbf{R}_{\mathrm{th},\parallel}$ is deduced as $\mathbf{R}_{\mathrm{th},\parallel} \sim -C_2\,(m_i/3.16\,T_i\tau_{\mathrm{s}})\,\mathbf{q}_{i,\parallel}^{\mathrm{PS}}$, $\mathbf{V}_{Z,\parallel} = V_{Z,\parallel}\mathbf{b}$ is the parallel flow velocity of the impurity:

$$V_{Z,\parallel} = V_{Z,\parallel}^{(1)} = \frac{1}{n_Z} \int \mathrm{d}^3 v\, v_\parallel\, \delta f_Z, \tag{6}$$

which should satisfy $|V_{Z,\parallel}/v_{\mathrm{th},Z}| \ll 1$, $v_{\mathrm{th},Z} = \sqrt{2T_Z/m_Z}$ is the thermal speed of the impurity, and τ_{s} is the slowing down time:

$$\tau_{\mathrm{s}} = \frac{12\pi^{3/2}}{\sqrt{2}} \frac{\sqrt{m_i}\,{T_i}^{3/2}{\epsilon_0}^2}{n_Z Z^2 e^4 \ln\Lambda}. \tag{7}$$

Here, ϵ_0 is the electric constant and $\ln\Lambda$ is the Coulomb logarithm. The coefficients C_1 and C_2 are given as $C_1 \approx 0.9$ and $C_2 \approx 1.89$, which are evaluated in [6]. Therefore, the term $C(f_{\mathrm{M},Z}, \delta f_i)$, which is called the field-particle collision term $C_{\mathrm{F}}^{Zi} f_{\mathrm{M},Z}$, is modelled by using the total force $\mathbf{R}_{Zi,\parallel}$ as follows [16],

$$C_{\mathrm{F}}^{Zi} f_{\mathrm{M},Z} := C(f_{\mathrm{M},Z}, \delta f_i) \approx \frac{R_{Zi,\parallel} v_\parallel}{n_Z T_Z} f_{\mathrm{M},Z}. \tag{8}$$

The term $C(\delta f_Z, f_{\mathrm{M},i})$ is called the test-particle collision term $C_{\mathrm{T}}^{Zi}\delta f_Z$:

$$C_{\mathrm{T}}^{Zi}\delta f_Z := C(\delta f_Z, f_{\mathrm{M},i}). \tag{9}$$

It should be noted that the characteristic time scale of $C_{\mathrm{T}}^{Zi}\delta f_Z$ is significantly smaller than the time scale of $C_{\mathrm{F}}^{Zi}f_{\mathrm{M},Z}$, as shown in section 1. This fact indicates difficulty in executing the impurity transport simulation with both terms $C_{\mathrm{F}}^{Zi}f_{\mathrm{M},Z}$ and $C_{\mathrm{T}}^{Zi}\delta f_Z$. On the other hand, the term $C_{\mathrm{T}}^{Zi}\delta f_Z$ has been usually ignored in the impurity transport analysis in a tokamak magnetic field, as shown, for example, in [4, 7]. In fact, in a circular tokamak field, the particle simulation including the binary Coulomb collision between the impurity and the background ion is not contradictory to the theoretical estimate obtained by taking account of only the total force $\mathbf{R}_{Zi,\parallel}$ [6]. As shown in section 2.3, we also confirm that the term $C_{\mathrm{T}}^{Zi}\delta f_Z$ does not play an important role as far as evaluating the radial particle flux of the impurity in the circular tokamak field, when the test-particle collision term is represented as $C_{\mathrm{T}}^{Zi}\delta f_Z = \nu_{\mathrm{D}}^{Zi}\mathscr{L}(\delta f_Z)$ for the sake of simplicity of the confirmation. Here, $\mathscr{L}$ is the Lorentz scattering operator and $\nu_{\mathrm{D}}^{Zi} \sim 1/\tau_{\mathrm{D}}^{Zi}$ is the deflection frequency of the impurity-ion collision:

$$\nu_{\mathrm{D}}^{Zi}(v) = \hat{\nu}_{Zi}\frac{\phi(x_i) - G(x_i)}{x_Z^3}, \tag{10}$$

where $\hat{\nu}_{ab} = n_b e_a^2 e_b^2 \ln\Lambda/(4\pi\epsilon_0^2 m_a^2 v_{\mathrm{th},a}^3)$, $\phi(x)$ is the error function $\mathrm{erf}(x)$, $G(x) = \{\phi(x) - x\phi'(x)\}/2x^2$, $x_a = v/v_{\mathrm{th},a}$, $e_Z = Ze$, and $e_i = e$ [16].

The self-collision term is expressed as

$$C(f_Z, f_Z) \approx C(f_{\mathrm{M},Z}, \delta f_Z) + C(\delta f_Z, f_{\mathrm{M},Z}). \tag{11}$$

The higher order term $C(\delta f_Z, \delta f_Z)$ is negligibly small compared to the other terms and is ignored in this paper. Therefore, the self-collision term is written as $C(f_Z, f_Z) = C_{\mathrm{F}}^{ZZ}f_{\mathrm{M},Z} + C_{\mathrm{T}}^{ZZ}\delta f_Z$, where $C_{\mathrm{F}}^{ZZ}f_{\mathrm{M},Z} := C(f_{\mathrm{M},Z}, \delta f_Z)$ and $C_{\mathrm{T}}^{ZZ}\delta f_Z := C(\delta f_Z, f_{\mathrm{M},Z})$ are called the field-particle and the test-particle collision terms, respectively. The self-collision term is usually considered not to play an important role in the impurity transport in a tokamak magnetic field. In section 2.3, the validity of ignoring the self-collision term is confirmed. For the sake of simplicity of the confirmation, the test-particle collision term is given as

$$C_{\mathrm{T}}^{ZZ}\delta f_Z = \nu_{\mathrm{D}}^{ZZ}(v)\,\mathscr{L}(\delta f_Z), \tag{12}$$

where $\nu_{\mathrm{D}}^{ZZ} \sim 1/\tau_{\mathrm{D}}^{ZZ}$ is the deflection frequency of the self-collision:

$$\nu_{\mathrm{D}}^{ZZ}(v) = \hat{\nu}_{ZZ}\frac{\phi(x_Z) - G(x_Z)}{x_Z^3}. \tag{13}$$

In this case, the field-particle collision term $C_{\mathrm{F}}^{ZZ}f_{\mathrm{M},Z}$ is given by the model operator which ensures the local momentum conservation property for the impurity-impurity collision, as shown in [16], i.e.,

$$C_{\mathrm{F}}^{ZZ}f_{\mathrm{M},Z} = \nu_{\mathrm{D}}^{ZZ}(v)\,\frac{m_Z}{T_Z}\mathbf{v}\cdot\mathbf{u}\,f_{\mathrm{M},Z}, \tag{14}$$

where the vector $\mathbf{u}$ is given as

$$\mathbf{u} = \int \mathrm{d}^3v\, \nu_{\mathrm{D}}^{ZZ}(v)\, \mathbf{v}\, \delta f_Z \Big/ \int \mathrm{d}^3v\, \nu_{\mathrm{D}}^{ZZ}(v)\, \frac{m_Z v^2}{3T_Z} f_{\mathrm{M},Z}. \tag{15}$$

From the discussions above, we have the following transport modelling:

$$\frac{\mathrm{D}\delta f_Z}{\mathrm{D}t} = \left\{ -\frac{\mathrm{D}}{\mathrm{D}t} + C_{\mathrm{F}}^{ZZ} + C_{\mathrm{F}}^{Zi} \right\} f_{\mathrm{M},Z}, \tag{16}$$

where $\mathrm{D}/\mathrm{D}t := \partial/\partial t + (\mathbf{v}_\parallel + \mathbf{v}_\mathrm{d}) \cdot \partial/\partial \mathbf{x} + \dot{v}_\parallel \partial/\partial v_\parallel - C_{\mathrm{T}}^{ZZ}$. Here, the role for the source/sink term S in the time evolution of δf_Z is ignored for the sake of benchmarks for comparing the simulation results with the results in the previous study [6]. The distribution function $f_Z = f_{\mathrm{M},Z} + \delta f_Z$ evolves with time from the Maxwellian function $f_{\mathrm{M},Z}$, i.e., $\delta f_Z = 0$ at $t = 0$ in equation (16). The condition of $|\delta f_Z / f_{\mathrm{M},Z}| \ll 1$, which means that $|\delta n_Z / n_Z| \ll 1$, $|\delta T_Z / T_Z| \ll 1$, and $|V_{Z,\parallel}/v_{\mathrm{th},Z}| \ll 1$, should be satisfied in this modelling. Here, δn_Z and δT_Z are given as

$$\delta n_Z = \overline{\left\langle \int \mathrm{d}^3v\, \delta f_Z \right\rangle} \tag{17}$$

and

$$\delta T_Z = \frac{1}{n_Z} \overline{\left\langle \int \mathrm{d}^3v\, \left\{ \frac{1}{3} m_Z v^2 - T_Z \right\} \delta f_Z \right\rangle}, \tag{18}$$

where $\overline{\cdot}$ means the time-average and $\langle\, \cdot\, \rangle$ is defined as $\langle\, \cdot\, \rangle = (1/\delta\mathcal{V}) \int_{\delta\mathcal{V}} \cdot\, \mathrm{d}^3x$. The small volume $\delta\mathcal{V}$ lies between the neighbouring magnetic flux surfaces. The two-weight δf method [18, 19] is applied to solve equation (16) as follows:

$$\begin{aligned} \frac{\mathrm{D}g}{\mathrm{D}t} &= 0, \\ \frac{\mathrm{D}w}{\mathrm{D}t} &= -\frac{\mathrm{D}p}{\mathrm{D}t} + \frac{p}{f_{\mathrm{M},Z}} C_{\mathrm{F}}^{ZZ} f_{\mathrm{M},Z} + \frac{p}{f_{\mathrm{M},Z}} C_{\mathrm{F}}^{Zi} f_{\mathrm{M},Z}, \\ \frac{\mathrm{D}p}{\mathrm{D}t} &= \frac{p}{f_{\mathrm{M},Z}} \frac{\mathrm{D}f_{\mathrm{M},Z}}{\mathrm{D}t}. \end{aligned} \tag{19}$$

The marker distribution function is expressed as g and the weight functions are w and p, which satisfy $wg = \delta f_Z$ and $pg = f_{\mathrm{M},Z}$. The marker particles, which are sample particles in the Monte-Carlo method, trace the guiding centre orbits. Here, the motions of the marker particles are given by the first equation of (19). As given from the second equation of (19), if the self-collision term can be ignored, then the time evolution of the weight w is given by integrating the following equation: $\mathrm{d}w/\mathrm{d}t = -\mathrm{d}p/\mathrm{d}t + (R_{Zi,\parallel} v_\parallel / n_Z T_Z)\, p$, where $\mathrm{d}/\mathrm{d}t := \partial/\partial t + (\mathbf{v}_\parallel + \mathbf{v}_\mathrm{d}) \cdot \partial/\partial \mathbf{x} + \dot{v}_\parallel \partial/\partial v_\parallel$. Note that the term $\mathrm{d}p/\mathrm{d}t$ is the contribution of $(\mathbf{v} \cdot \nabla r)\, \partial f_{\mathrm{M},Z}/\partial r$ and the term $(R_{Zi,\parallel} v_\parallel / n_Z T_Z)\, p$ is the contribution of $C(f_{\mathrm{M},Z}, \delta f_i)$. Here, r is a label of the magnetic flux surfaces. The simulation model described by equation (19) is implemented in the drift-kinetic δf simulation code, KEATS [13, 14]. Benchmarks of the simulation code are shown in the next section.

2.2. Benchmarks of the simulation code

Setting of simulation conditions is given as follows. The magnetic configuration used in benchmarks of the simulation code is set to a circular tokamak field, which is essentially the same as in the previous study [6]. The major radius of the magnetic axis is $R_{\rm ax} = 3$ or 12 m, the minor radius of the toroidal plasma is $a = 1$ m, and the strength of the magnetic field on the magnetic axis is $B_{\rm ax} = 3$ T. The circular tokamak field $\mathbf{B} = B_R\widehat{R} + B_\varphi\widehat{\varphi} + B_z\widehat{z}$ is given by $B_R = B_{\rm ax}z/qR$, $B_\varphi = -B_{\rm ax}R_{\rm ax}/R$, and $B_z = -B_{\rm ax}(R - R_{\rm ax})/qR$ in the cylindrical coordinates (R, φ, z). Here, the safety factor q is set to $q = q(r) = \max\{q_0, 2\pi B_{\rm ax}r^2/(\mu_0 R_{\rm ax}I_2)\}$, $q_0 = q(r/a = 0.1)$, $r = \sqrt{(R - R_{\rm ax})^2 + z^2}$ is the minor radius, μ_0 is the magnetic permeability, and $I_2 = 1.2$ MA in the case of $R_{\rm ax} = 3$ m or 0.3 MA in the case of $R_{\rm ax} = 12$ m. Note that the case of $R_{\rm ax} = 12$ m is considered in the benchmark of comparison between the simulation result and the theoretical estimate under the assumption of large aspect ratio. For the sake of simplicity of the benchmarks, the number density and the temperature of the impurity are set to $n_Z = n_0 - (n_0 - n_a)r/a$ and $T_Z = T_i$. Here, $n_0 = 0.86 \times 10^{15}$ m^{-3} and $n_a = 1.2n_0$. The number density and the temperature of the background ion are assumed to be $n_i = 3 \times 10^{19}$ m^{-3} and $T_i = 100$ eV. In addition, the gradients of n_i and T_i are considered as $\partial \ln n_i/\partial r = -1/5a$ and $\partial \ln T_i/\partial r = -1/5a$. The PS flow velocity and the PS heat flux of the background ion are given as $V_{i,\parallel}^{\rm PS} \approx (2q/n_i eB)(\mathrm{d}p_i/\mathrm{d}r)\cos\theta$ and $q_{i,\parallel}^{\rm PS} \approx (5qn_iT_i/eB)(\mathrm{d}T_i/\mathrm{d}r)\cos\theta$, where $p_i = n_iT_i$ and θ is the poloidal angle given by $R - R_{\rm ax} = r\cos\theta$ and $z = r\sin\theta$. The marker particles used in the simulations are distributed initially and uniformly in the region of $r/a < 1.05$ in the torus. The marker particles are absorbed when arriving at the wall of the calculation box, which is set to $|R - R_{\rm ax}|/a < 1.5$, $0 < \varphi/2\pi < 1$, and $|z|/a < 1.5$ for all the simulations. The function g in equation (19) is given approximately by the distribution function of the marker particles. In the simulations in this paper, the charge number of the W impurity is set to $Z = +4$, which is the same value as in the previous study [6].

We should note that the charge number Z depends on the electron temperature. If the electron temperature is ~ 100 eV, then the charge number Z of W impurity is ~ 14, as shown in [20]. Here, the number density of electrons is set to $n_e \sim 3\times10^{19}$ m^{-3}. In the previous study [6], the charge number Z was set to be 4 because the full-orbit particle simulation is highly time-consuming. Here, the calculation cost of the full-orbit particle simulation is strongly related to the gyrofrequency of the W impurity particle. Setting of the ionization stage $Z = +4$ corresponds to the case that the electron temperature is ~ 10 eV. For the sake of applicability of the benchmarks, the charge number Z is also set to be 4 in this paper. This is because the simple formula of the friction and the thermal forces in equation (5) was confirmed in the case of $Z = +4$ in the previous study [6]. The purpose of the benchmarks is to check the developed code and to show the difference between the simulation result and the theoretical estimate under almost the same simulation conditions as in the previous study [6]. This is also because of clarifying the improvement of the present simulation study from the previous study.

The difference mentioned above, which is caused by the global effect, is not peculiar to the case of $Z = +4$.

If the distribution function of the impurity is very close to the Maxwellian function, i.e., $f_Z \approx f_{\mathrm{M},Z}$, then the parallel flow velocity of the impurity is approximately given as $V_{Z,\parallel} = V_{Z,\parallel}^{\mathrm{PS}} \approx (2q/n_Z ZeB)(\mathrm{d}p_Z/\mathrm{d}r)\cos\theta$ [21], where $p_Z = n_Z T_Z$. Note that $V_{Z,\parallel}^{\mathrm{PS}}$ has the opposite direction to $V_{i,\parallel}^{\mathrm{PS}}$ because of the difference between the gradients of p_Z and p_i. Then, the theoretical estimate of the radial particle flux, which is derived in the previous study [6], is written as

$$\left\langle \Gamma_r^{\mathrm{theory}} \right\rangle = \frac{2q^2}{m_i \Omega_i^2 \tau_{\mathrm{s}}} \left\{ \frac{C_1}{Z} \frac{\mathrm{d}p_i}{\mathrm{d}r} - \frac{C_1\, n_i}{Z^2\, n_Z} \frac{\mathrm{d}p_Z}{\mathrm{d}r} - \frac{5}{2 \times 3.16} \frac{C_2\, n_i}{Z} \frac{\mathrm{d}T_i}{\mathrm{d}r} \right\} \tag{20}$$

under the approximations of the large aspect ratio and $V_{Z,\parallel} = V_{Z,\parallel}^{\mathrm{PS}}$, where $\Omega_i = eB/m_i$.

The first benchmark is the check whether the simulation under the following constraint is consistent with the theoretical estimate. Here, the constraint is that instead of equation (6), $V_{Z,\parallel}^{\mathrm{PS}}$ is substituted into $V_{Z,\parallel}$ in the evaluation of the term $C_{\mathrm{F}}^{Zi} f_{\mathrm{M},Z}$ (i.e., equation (8)). In the simulation, the radial particle flux is given as

$$\langle \Gamma_r \rangle = \overline{\left\langle \int \mathrm{d}^3 v\ (\mathbf{v} \cdot \nabla r)\ f_Z \right\rangle} = \left\langle \Gamma_r^{(0)} \right\rangle + \left\langle \Gamma_r^{(1)} \right\rangle, \tag{21}$$

where $\mathbf{v} = \mathbf{v}_\parallel + \mathbf{v}_{\mathrm{d}}$, $\left\langle \Gamma_r^{(0)} \right\rangle = \overline{\left\langle \int \mathrm{d}^3 v\ (\mathbf{v} \cdot \nabla r)\ f_{\mathrm{M},Z} \right\rangle}$, and $\left\langle \Gamma_r^{(1)} \right\rangle = \overline{\left\langle \int \mathrm{d}^3 v\ (\mathbf{v} \cdot \nabla r)\ \delta f_Z \right\rangle}$. Here, $\left\langle \Gamma_r^{(0)} \right\rangle$ should be zero. As shown in figure 1, we confirm that the simulation results of $\left\langle \Gamma_r^{(0)} \right\rangle$ and $\left\langle \Gamma_r^{(1)} \right\rangle$ are in agreement with the theoretical estimates. This result is obtained regardless of the time t.

The parallel flow velocity $V_{Z,\parallel}$ should be determined by the distribution function of the impurity, as shown in equation (6), and thus the radial particle flux of the impurity is recalculated without the constraint of $V_{Z,\parallel} = V_{Z,\parallel}^{\mathrm{PS}}$ in the evaluation of equation (8). In the case of $t/\tau_{\mathrm{s}} \lesssim 1$, which is set in the previous study [6] in order to confirm the validity of the simple formula (5) by the full-orbit particle simulation, the radial particle flux $\left\langle \Gamma_r^{(1)} \right\rangle$ is close to the theoretical estimate, as shown in figure 2. This is because $f_Z \sim f_{\mathrm{M},Z}$ and $V_{Z,\parallel} \sim V_{Z,\parallel}^{\mathrm{PS}}$ even in the recalculation without the constraint.

2.3. Drift-kinetic simulation beyond the condition of $t/\tau_{\mathrm{s}} \lesssim 1$

After $t/\tau_{\mathrm{s}} \sim 1$, we see the differences between the previous and the present studies. The radial particle flux $\left\langle \Gamma_r^{(1)} \right\rangle$ leaves slowly from the theoretical estimate and relaxes after ten or more times longer than the slowing down time τ_{s}, as shown in figure 3. From this result, it is seen that the simulation result of $\left\langle \Gamma_r^{(1)} \right\rangle$ differs visibly from the theoretical estimate after a sufficient amount of time. Here, we confirm that $|\delta n_Z/n_Z|, |\delta T_Z/T_Z| \lesssim 1/20$ in the simulation, and that the number of the marker particles which are absorbed at the wall of the calculation box is less than 9×10^{-3} % of the total amount ($= 6.4 \times 10^7$). The mechanism of the relaxation shown in figure 3 is explained by the time integral of the weight w along the guiding centre orbits

across the neighbouring magnetic flux surfaces. Considering the case of a fixed initial velocity, the periods of the passing particles and the trapped particles become long in general as the initial positions of the guiding centres in the core are close to the edge of $r/a = 1$. Thus, the relaxation is affected by the different periods depending on the initial positions. Note that it is most important to evaluate the radial particle flux by the sufficiently relaxed δf_Z because the distribution function $f_Z = f_{\mathrm{M},Z} + \delta f_Z$ should be quasi-steady in the simulation model proposed in this paper. Note also that, as shown in figure 4, the radial particle flux after the sufficient time in the simulation does not depend on the self-collision term.

As shown in figure 5, the parallel flow velocity of the impurity in the simulation after the sufficient time changes for reducing $\left| V_{Z,\parallel} - V_{i,\parallel}^{\mathrm{PS}} \right|$, i.e., for reducing the friction force, which is the first term in equation (5), especially in the edge region of $r/a \gtrsim 0.8$. As a result, the negative radial particle flux is reduced by the thermal force unchanged after the sufficient time. Here, the roles of the friction and the thermal forces are discussed in the previous study [6]. Note that the time evolution of the weight w is given as $\mathrm{d}w/\mathrm{d}t \approx -\mathrm{d}p/\mathrm{d}t + (R_{Zi,\parallel} v_\parallel / n_Z T_Z)\, p$, and that the thermal force, which is the second term in equation (5), is independent from δf_Z. It is known that the neoclassical inward pinch is caused by the friction force, and the neoclassical temperature screening effect originates mainly from the thermal force [6, 10].

The poloidal dependence of the radial particle flux is illustrated in figure 6. This result shows the inflow of the impurity from the top part of the torus and the outflow from the bottom part. This is consistent with the results in [6, 7]. Here, the poloidal dependence is given from $\Gamma_r^{(1)} = \int \mathrm{d}^3 v\, (\mathbf{v} \cdot \nabla r)\, \delta f_Z$. The function $\delta f_Z = wg$ is evaluated from the time integral of the following equation along the guiding centre orbits: $\mathrm{d}w/\mathrm{d}t \approx -\mathrm{d}p/\mathrm{d}t + (R_{Zi,\parallel} v_\parallel / n_Z T_Z)\, p$.

We should note that the self-collision term does not play an important role in all the results shown in figures 4, 5, and 6. Therefore, the self-collision term is negligible for the evaluation of the radial particle flux of the impurity in the circular tokamak field. Hereafter, the self-collision term is ignored.

The impurity has a finite orbit width of its guiding centre, which is typically $\lesssim 1$ cm. The time evolution of the weight w is given by integrating $\mathrm{d}w/\mathrm{d}t = -\mathrm{d}p/\mathrm{d}t + (R_{Zi,\parallel} v_\parallel / n_Z T_Z)\, p$ along the guiding centre orbit across the neighbouring magnetic flux surfaces. Note that δf_Z is represented as $\delta f_Z(t, \mathbf{x}, \mathbf{v}) = \sum_j w_j(t)\, \delta(\mathbf{x} - \mathbf{x}_j(t))\, \delta(\mathbf{v} - \mathbf{v}_j(t))$, where $w_j(t)$ is the weight w of the j-th marker particle and the guiding centre orbit of the j-th marker particle is expressed as $(\mathbf{x}_j(t), \mathbf{v}_j(t))$. Hence, the evaluation of δf_Z on an arbitrary magnetic flux surface cannot be independent from the friction and the thermal forces, which are given by equations (5) and (6), on the neighbouring magnetic flux surfaces because the orbit width is non-zero. Here, this friction force depends on the values of δf_Z on the neighbouring magnetic flux surfaces through the parallel flow velocity $V_{Z,\parallel}$. It is natural that the evaluation of the radial particle flux depends on the simulation conditions in the region of $r/a > 1$, which can be defined by the initial distribution of the marker particles used in the simulation without the self-collision

term in this paper. In fact, for example, when the region where the marker particles are initially distributed changes from $r/a < 1.05$ to $r/a < 1.20$, the flux $\left\langle \Gamma_r^{(1)} \right\rangle$ and the parallel flow velocity $V_{Z,\parallel}$ in the quasi-steady state of δf_Z become changed as shown in figures 7 and 8. In addition, the changes of $\left\langle \Gamma_r^{(1)} \right\rangle$ and $V_{Z,\parallel}$ from the theoretical estimates become large as the magnetic flux surface of evaluating δf_Z is close to the boundary of $r/a = 1.05$ or 1.20, and also become small for separating the boundary from the edge of $r/a = 1$. Therefore, the solution δf_Z (and also the flux $\left\langle \Gamma_r^{(1)} \right\rangle$) on a magnetic flux surface is influenced by the simulation conditions and the values of the solution δf_Z all over the edge region including the region of $r/a > 1$. In this paper, this is called the global effect on the impurity transport. If the finite orbit width is ignored in the simulation, the difference between the simulation result and the theoretical estimate disappears, as shown in appendix.

Finally, we investigate the effect of the test-particle collision term $C_{\mathrm{T}}^{Zi}\delta f_Z$, which is ignored in the benchmarks above. It is difficult to calculate directly the value of the flux $\left\langle \Gamma_r^{(1)} \right\rangle$ including the effect of $C_{\mathrm{T}}^{Zi}\delta f_Z$ because the simulation becomes highly time consuming. Instead of the direct calculation, the effect of $C_{\mathrm{T}}^{Zi}\delta f_Z = \nu_{\mathrm{D}}^{Zi}\mathscr{L}(\delta f_Z)$ is investigated asymptotically, i.e., the cases of $(\nu_{\mathrm{D}}^{Zi}/100)\mathscr{L}(\delta f_Z)$ and $(\nu_{\mathrm{D}}^{Zi}/10)\mathscr{L}(\delta f_Z)$ are examined. From the asymptotic investigation, the radial particle flux of the impurity is not strongly affected by the test-particle collision term $C_{\mathrm{T}}^{Zi}\delta f_Z$, as shown in figure 9. Here, if $t/\tau_s \lesssim 1$, it is possible to perform the simulation for the case of $\nu_{\mathrm{D}}^{Zi}\mathscr{L}(\delta f_Z)$, and thus the result is shown in figure 9(a). There is no significant dependence of the fluxes $\left\langle \Gamma_r^{(1)} \right\rangle$ on the term $C_{\mathrm{T}}^{Zi}\delta f_Z$ at $t/\tau_{\mathrm{s}} \lesssim 1$, and also after the sufficient time. Note that the slowing down time τ_{s} is sufficiently longer than the deflection time τ_{D}^{Zi}, as shown in section 1. It is confirmed that the test-particle collision term $C_{\mathrm{T}}^{Zi}\delta f_Z$ is negligible for the evaluation of the flux $\left\langle \Gamma_r^{(1)} \right\rangle$ in the circular tokamak field.

3. Summary and discussion

The global modelling of tungsten impurity transport is developed for evaluating the radial particle flux $\left\langle \Gamma_r^{(1)} \right\rangle$ of the impurity in the edge region of a tokamak plasma, based on the drift-kinetic equation of the impurity having a charge number Z. The number density of the impurity is required to be 10^4-10^5 times smaller than the number density of the background ion in the edge region. Thus it is not practical to execute a kinetic simulation treating time evolution of all the species of plasma particles because of the excessive differences between the characteristic time scales. Hence, the collisional transport model should be simplified. The distribution function f_i of the background ion is assumed to be determined independently of the distribution function f_Z of the impurity, and f_i is represented by using the 13-moments approximation. Here, the collisionality of the background ion is in the Pfirsch-Schlüter regime. The Coulomb collision between the impurity and the background ion is simplified by the friction force and the thermal force on the impurity particles in the parallel directions. The model is

implemented in the drift-kinetic δf simulation code, KEATS [13, 14]. It is confirmed that the radial particle flux is dominated by the friction force and the thermal force acting on the impurity particles along magnetic field lines. The radial diffusion caused by the self-collision of the impurity and the test-particle collision between the impurity and the background ion does not play an important role for evaluating the flux $\left\langle \Gamma_r^{(1)} \right\rangle$. These results are consistent with the results in the previous study [6]. The knowledge obtained in [6] is confirmed for the trace impurity with the low charge number. However, its application range is not clear yet. More research is needed to investigate the application range under various conditions of the magnetic configuration, the number density of the impurity and so on.

In addition to the knowledge obtained in the previous studies [5, 6], it is found that the global effect caused by the guiding centre motions is not negligible in the evaluation of the flux $\left\langle \Gamma_r^{(1)} \right\rangle$. After the sufficient time $t/\tau_{\rm s} \gtrsim 10$, the distribution function f_Z relaxes sufficiently, and the flux $\left\langle \Gamma_r^{(1)} \right\rangle$ in the drift-kinetic δf simulation differs visibly from the theoretical estimate obtained under ignoring the global effect, as shown in figure 3. Here, $\tau_{\rm s}$ is the slowing down time. The solution δf_Z of the drift-kinetic equation (and also the radial particle flux $\left\langle \Gamma_r^{(1)} \right\rangle$) on a magnetic flux surface is influenced by the simulation conditions and the values of the solution δf_Z all over the edge region including the region of $r/a > 1$, as shown in figures 7 and 8. This global effect is caused by the magnetic drift term in the left-hand side of equation (16) including the friction force and the thermal force. See also appendix.

We should note the following. As shown in appendix, the value of $\left\langle \Gamma_r^{(1)} \right\rangle$ does not depend on the values themselves of the orbit widths, where the typical orbit width is, for example, the banana width of a particle moving at the thermal speed. On the other hand, the relaxation time of parallel flow velocity is affected by the orbit widths because of the mechanism of the global effect explained in section 2.3. If the charge number $Z \gg 1$, then the typical orbit width $\Delta_{\rm orbit}$ is quite small, and the relaxation time is extremely long compared to the slowing down time $\tau_{\rm s}$. When $\Delta_{\rm orbit} \to 0$, the relaxation time becomes ∞. Then the global effect is practically negligible because the global effect appears after the relaxation time, as shown in figure 3, and because the relaxation time that is longer than the discharge time is meaningless. When the electron temperature is > 100 eV, the global effect on the W accumulation might be negligible, depending on the discharge time. On the other hand, if the electron temperature around the edge of $r/a = 1$ is sufficiently low, for example, the order of ~ 10 eV, then the global effect on the impurity transport around the edge should be considered because the radial particle flux changes visibly from the theoretical estimate.

In the edge region of the tokamak plasma in this paper, the friction and the thermal forces strongly affect the time evolution of the distribution function f_Z. On the other hand, when the impurity transport is considered in the edge region of a helical plasma in a low collisionality regime, the test-particle collision between the impurity and the background ion, $C(\delta f_Z, f_{{\rm M},i})$, and the collisions between the impurities having various

charge numbers Z and Z', $C(f_Z, f_{Z'})$, should not be ignored in the evaluation of the radial particle flux because of the neoclassical diffusion caused by the helical ripples (e.g., recall the neoclassical transport in the $1/\nu$ regime). In addition, effects of an ambipolar electric field should also be considered in the helical plasma [22]. There also are other topics. For example, the evaluation of the radial particle flux requires appropriate simulation conditions in the core and the region of $r/a > 1$, which should be determined by the collisional transport between the scrape-off layer and the core region. Further investigations regarding these topics will be performed in the near future.

Acknowledgments

The authors are particularly grateful for the discussions with Dr. Seikichi Matsuoka on the local modelling of the neoclassical transport. Based on the discussions, the results in appendix were obtained. The computational simulations in this paper were conducted using the supercomputers "Plasma Simulator" at National Institute for Fusion Science (NIFS) and "Japan Fusion Reactor Simulator 1" at Computational Simulation Centre of International Fusion Energy Research Centre (IFERC-CSC) in Rokkasho Fusion Institute of QST (Aomori, Japan). This work was performed with the support and under the auspices of the NIFS Collaborative Research Programs "NIFS16KNTT038", "NIFS17KNST109", "NIFS19KNTT052", and "NIFS19KNST142", the IFERC-CSC project "DKSOIT", and the FLAGSHIP2020, MEXT within the priority study 6.

Appendix. Local and global modelling of impurity transport

The neoclassical transport theory is based on the drift-kinetic equation and usually employs the assumption of ignoring the magnetic drift term $(\mathbf{v} - v_\parallel \mathbf{b}) \cdot \partial\, \delta f_Z / \partial\, \mathbf{x}$ in the left-hand side of equation (16) [16, 21], where $\mathbf{v} = \mathbf{v}_\parallel + \mathbf{v}_\mathrm{d}$. This assumption is often called the zero magnetic drift (ZMD) limit [23, 24]. The drift-kinetic equation in the ZMD limit is expressed as

$$\left\{ \frac{\partial}{\partial t} + v_\parallel \mathbf{b} \cdot \frac{\partial}{\partial \mathbf{x}} + \dot{\xi} \frac{\partial}{\partial \xi} \right\} \delta f_Z = S_0(f_{\mathrm{M},Z}) + C_\mathrm{F}^{Zi} f_{\mathrm{M},Z}, \tag{A1}$$

where $\dot{\xi} = \mathrm{d}(v_\parallel / v)/\mathrm{d}t$ is approximately represented as $\dot{\xi} = -\{(1-\xi^2)v/2B\}\mathbf{b} \cdot \nabla B$ in this model, $\dot{v} = 0$, and $\nabla = \partial/\partial \mathbf{x}$. The term S_0 is given as $S_0 = -(\mathbf{v} \cdot \nabla r)\, \partial f_{\mathrm{M},Z}/\partial r$, r is a label of the magnetic flux surfaces, and $f_{\mathrm{M},Z} = f_{\mathrm{M},Z}(r, v)$. Note that the right-hand side in equation (A1) is the same as in the right-hand side of equation (16). Here, the terms $C_\mathrm{T}^{ZZ} \delta f_Z$ and $C_\mathrm{F}^{ZZ} f_{\mathrm{M},Z}$ in (16) are ignored in (A1). This initial value problem (A1) with the condition $\delta f_Z = 0$ at $t = 0$ can be solved independently on each magnetic flux surface because the equations of motion include $\dot{r} = 0$ in the left-hand side of (A1). When magnetic flux coordinates are used in a solver of the problem (A1), the solver should be based on the numerical methods given in [23, 24]. On the other hand, in KEATS code in this paper, Eulerian coordinates are used for describing the configuration space. The 5-dimensional phase space is written as $\boldsymbol{\zeta} = (u^1, u^2, u^3, v, \xi)$, where $u^1 = R - R_\mathrm{ax}$, $u^2 = z$, and $u^3 = -\varphi$. Here, (R, φ, z) is the cylindrical coordinates. In equation (A1), the equations of motion are described as

$$\frac{\mathrm{d}u^1}{\mathrm{d}t} = v\xi b^1, \tag{A2.a}$$

$$\frac{\mathrm{d}u^2}{\mathrm{d}t} = v\xi b^2, \tag{A2.b}$$

$$\frac{\mathrm{d}u^3}{\mathrm{d}t} = v\xi b^3, \tag{A2.c}$$

$$\frac{\mathrm{d}v}{\mathrm{d}t} = 0, \tag{A2.d}$$

$$\frac{\mathrm{d}\xi}{\mathrm{d}t} = -\frac{(1-\xi^2)v}{2B}\, \mathbf{b} \cdot \nabla B, \tag{A2.e}$$

where $b^k = \mathbf{b} \cdot \nabla u^k$ and $k = 1, 2, 3$. These equations of motion do not satisfy the Liouville's theorem, i.e., the compressibility of the phase-space volume is produced as $\nabla_\zeta \cdot \dot{\boldsymbol{\zeta}} = v\xi b^1/(R_\mathrm{ax} + u^1)$, where $\nabla_\zeta = \partial/\partial\boldsymbol{\zeta}$. As shown in [23, 24], the time evolution of the weights w and p are given as

$$\frac{\mathrm{d}w}{\mathrm{d}t} = (\nabla_\zeta \cdot \dot{\boldsymbol{\zeta}})\, w + \left(\frac{p}{f_{\mathrm{M},Z}} \right) S_0 + C_\mathrm{F}^{Zi} p, \tag{A3.a}$$

$$\frac{\mathrm{d}p}{\mathrm{d}t} = (\nabla_\zeta \cdot \dot{\boldsymbol{\zeta}})\, p. \tag{A3.b}$$

Here, the marker particles are distributed initially and uniformly in the region of

$r/a < 1.05$. The model mentioned above is often called the local model [23, 24], and in this model the function δf_Z is evaluated independently on each magnetic flux surface having the small volume $\delta\mathcal{V}$. As a matter of course, the radial particle flux $\left\langle \Gamma_r^{(1)} \right\rangle$ evaluated by using KEATS code based on the local model is in agreement with the theoretical estimate (20) after sufficient time ($t/\tau_{\rm s} \gtrsim 6$ in this case), as shown in figure A1. Here, the simulation conditions in figure A1 are the same as in section 2.2. Hence, the difference between the simulation result and the theoretical estimate in figure 4 (and also in figure A5 shown below) is caused by the magnetic drift term in the left-hand side of equation (16). This fact provides definite evidence of the global effect, which originates from the finite orbit widths of guiding centres, as explained in section 2.3. Note that the finite orbit widths of guiding centres across the neighbouring magnetic flux surfaces are generated by the magnetic drift term.

We should note that the magnetic drift term in the left-hand side of the drift-kinetic equation (16) does not usually cause unignorable differences from theoretical estimates based on the local model ignoring the magnetic drift term. For example, when the terms of the friction and the thermal forces and the self-collision terms are ignored in equation (16), the parallel flow velocity $V_{Z,\parallel}^{(1)} - \left\langle V_{Z,\parallel}^{(1)} \right\rangle$ and the parallel heat flux $q_{Z,\parallel}^{(1)} - \left\langle q_{Z,\parallel}^{(1)} \right\rangle$ in the simulation based on (19) are in good agreement with the theoretical estimates, i.e., the Pfirsch-Schlüter (PS) flow velocity and the PS heat flux, as shown in figure A2. Here, $V_{Z,\parallel}^{(1)} = (1/n_Z)\int {\rm d}^3v\, v_\parallel\, \delta f_Z$ and $q_{Z,\parallel}^{(1)} = \int {\rm d}^3v\, \{(1/2)m_Z v^2 - (5/2)T_Z\}\, v_\parallel\, \delta f_Z$. In the simulation in figure A2, the profiles of the number density n_Z and the temperature T_Z are set to $n_Z = n_0 - (n_0 - n_a)r/a$ and $T_Z = T_0 - (T_0 - T_a)r/a$, where $n_0 = 0.86 \times 10^{15}$ m^{-3}, $T_0 = 119.05$ eV, $n_a = 1.2n_0$, and $T_a = 0.8T_0$. This result also confirms that the PS flow velocity and the PS heat flux are given from the contribution of δf_Z generated by the term $S_0 = -(\mathbf{v}\cdot\nabla r)\,\partial f_{{\rm M},Z}/\partial r$ in the right-hand side of equation (16).

The term $C_{\rm F}^{Zi}p$ is associated with the friction and the thermal forces (5). Considering $C_{\rm F}^{Zi}p$, the weight w becomes different from w in the case of ignoring $C_{\rm F}^{Zi}p$. Through the function $\delta f_Z = wg$, the parallel flow velocity $V_{Z,\parallel}^{(1)}$ differs from the PS flow velocity, as shown in figures 5 and 8. It should be noted that in the simulation based on the local model in figure A1, the parallel flow velocity is negligibly affected by the term $C_{\rm F}^{Zi}p$, as shown in figure A3(a). This result means that the parallel flow velocity in the local model is well approximated by the PS flow velocity, and thus the assumption of using the PS flow velocity is confirmed to be appropriate in the theoretical estimate. In order to compare the parallel flow velocities in the cases of considering and ignoring $C_{\rm F}^{Zi}p$ in the local model, $V_{Z,\parallel}^{(1)} - \left\langle V_{Z,\parallel}^{(1)} \right\rangle$ in the case of ignoring $C_{\rm F}^{Zi}p$ is also shown in figure A3(b).

We should note that the label of the magnetic flux surfaces, in particular, in the circular tokamak field is given by $r = \sqrt{(u^1)^2 + (u^2)^2}$. In this case, it is possible to consider a solver employing the coordinates $(r, \theta, \phi, v, \xi)$, where $\phi = u^3$ and θ is given by $\cos\theta = u^1/r$ and $\sin\theta = u^2/r$. The guiding centre orbit in the 4-dimensional phase space $\boldsymbol{\zeta} = (\theta, \phi, v, \xi)$ satisfies $\nabla_\zeta \cdot \dot{\boldsymbol{\zeta}} = 0$ because of $\dot{r} = 0$ [23, 24], and thus the time

evolution of the weights w and p in this modelling are given as

$$\frac{\mathrm{d}w}{\mathrm{d}t} = \left(\frac{p}{f_{\mathrm{M},Z}}\right) S_0 + C_{\mathrm{F}}^{Zi} p, \tag{A4.a}$$

$$\frac{\mathrm{d}p}{\mathrm{d}t} = 0. \tag{A4.b}$$

Here, the marker particles satisfying the equations above are distributed initially and uniformly on selected magnetic flux surfaces in the region of $r/a < 1$. We confirm that the radial particle flux $\left\langle \Gamma_r^{(1)} \right\rangle$ evaluated by using KEATS code based on another local modelling above is in agreement with the theoretical estimate (20) after sufficient time, as shown in figure A4. Here, the simulation conditions in figure A4 are the same as in figure A1.

Finally, for understanding the difference between the "local" and the "global" models in this paper, the equations of motion and the time evaluation of the weights w and p in the global model (19) based on equation (16) are described as follows:

$$\frac{\mathrm{d}u^1}{\mathrm{d}t} = \mathbf{v} \cdot \nabla u^1, \tag{A5.a}$$

$$\frac{\mathrm{d}u^2}{\mathrm{d}t} = \mathbf{v} \cdot \nabla u^2, \tag{A5.b}$$

$$\frac{\mathrm{d}u^3}{\mathrm{d}t} = \mathbf{v} \cdot \nabla u^3, \tag{A5.c}$$

$$\frac{\mathrm{d}v}{\mathrm{d}t} = 0, \tag{A5.d}$$

$$\frac{\mathrm{d}v_\parallel}{\mathrm{d}t} = -\left(\frac{\mu}{m_Z B_\parallel^*}\right) \mathbf{B}^* \cdot \nabla B, \tag{A5.e}$$

$$\frac{\mathrm{d}w}{\mathrm{d}t} = -\frac{\mathrm{d}p}{\mathrm{d}t} + C_{\mathrm{F}}^{Zi} p, \tag{A5.f}$$

$$\frac{\mathrm{d}p}{\mathrm{d}t} = \frac{p}{f_{\mathrm{M},Z}} \frac{\mathrm{d}f_{\mathrm{M},Z}}{\mathrm{d}t}. \tag{A5.g}$$

As shown in section 2.1, $\mathbf{v} = \mathbf{v}_\parallel + \mathbf{v}_\mathrm{d}$, $\mathbf{v}_\parallel = v_\parallel \mathbf{B}^*/B_\parallel^*$, $\mathbf{v}_\mathrm{d} = \{(\mu/Ze)\mathbf{b} \times \nabla B\}/B_\parallel^*$, $\mu = m_Z {v_\perp}^2/2B$, $v_\perp = \sqrt{v^2 - {v_\parallel}^2}$, $\mathbf{B}^* = \mathbf{B} + (m_Z v_\parallel/Ze)\nabla \times \mathbf{b}$, and $B_\parallel^* = \mathbf{b} \cdot \mathbf{B}^*$ [15, 16]. The self-collision terms are ignored. The simulation result of $\left\langle \Gamma_r^{(1)} \right\rangle$ based on this global model in the case of $R_{\mathrm{ax}}/a = 12$ is shown in figure A5. Here, the marker particles are distributed initially and uniformly in the region of $r/a < 1.05$. The simulation result in the case of $R_{\mathrm{ax}}/a = 12$ is in agreement with the simulation result in the case of $R_{\mathrm{ax}}/a = 3$. Hence, the value of $\left\langle \Gamma_r^{(1)} \right\rangle$ does not depend on the values themselves of the orbit widths. In the concept of the global effect on the impurity transport, it is important that the orbit widths are non-zero, as explained in section 2.3. Note that the relaxation time of parallel flow velocity depends on the orbit widths, where the typical orbit width is, for example, the banana width of a particle moving at the thermal speed. In fact, in figure A5 the relaxation time in the case of $R_{\mathrm{ax}}/a = 3$ is approximately two

times in the case of $R_{\mathrm{ax}}/a = 12$ because the typical orbit width in the case of $R_{\mathrm{ax}}/a = 3$ is approximately one half of the typical orbit width in the case of $R_{\mathrm{ax}}/a = 12$.

References

[1] Helander P. *et al* 2017 *Phys. Rev. Lett.* **118** 155002
[2] Nakano T. *et al* 2009 *Nucl. Fusion* **49** 115024
[3] Philipps V. 2011 *J. Nucl. Matter.* **415** 52
[4] Shimizu K. *et al* 1997 *J. Nucl. Mater.* **241-243** 167
[5] Homma Y. *et al* 2013 *J. Comput. Phys.* **250** 206
[6] Homma Y. *et al* 2016 *Nucl. Fusion* **56** 036009
[7] Yamoto S. *et al* 2017 *Nucl. Fusion* **57** 116051
[8] Keilhacker M. *et al* 1991 *Nucl. Fusion* **31** 535
[9] Matthews G.F. *et al* 1992 *J. Nucl. Mater.* **196-198** 374
[10] Hirshman S.P. and Sigmar D.J. 1981 *Nucl. Fusion* **21** 1079
[11] Pusztai I. *et al* 2016 *Plasma Phys. Control. Fusion* **58** 085001
[12] Chang C.S. *et al* 2004 *Phys. Plasmas* **11** 2649
[13] Nunami M. *et al* 2007 *Research Report NIFS Series* No.NIFS-871
[14] Kanno R. *et al* 2008 *Plasma Fusion Res.* **3** S1060
[15] Littlejohn R.G. 1983 *J. Plasma Phys.* **29** 111
[16] Helander P. and Sigmar D.J. 2002 *Collisional Transport in Magnetized Plasmas* (Cambridge: Cambridge Univ. Press)
[17] Golant V.E. *et al* 1977 *Fundamentals of Plasma Physics* (New York: Wiley)
[18] Wang W.X. *et al* 1999 *Plasma Phys. Control. Fusion* **41** 1091
[19] Brunner S. *et al* 1999 *Phys. Plasmas* **6** 4504
[20] See the atomic molecular data services provided by the nuclear data section in IAEA (https://www-amdis.iaea.org/computing.php); Chung H.-K., Chen M.H., Morgan W.L., Ralchenko Y. and Lee R.W. 2005 *High Energy Dens. Phys.* **1** 3
[21] Hazeltine R.D. *et al* 1973 *Phys. Fluids* **16** 1645
[22] Calvo I. *et al* 2018 *Nucl. Fusion* **58** 124005
[23] Matsuoka S. *et al.*, 2015 *Phys. Plasmas* **22** 072511
[24] Huang B. *et al.*, 2017 *Phys. Plasmas* **24** 022503

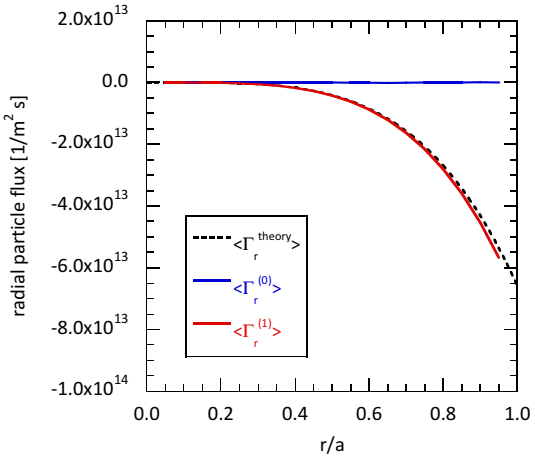

Figure 1. The theoretical estimate of the radial particle flux is illustrated by the black dashed line. The radial particle fluxes $\left\langle \Gamma_r^{(0)} \right\rangle$ and $\left\langle \Gamma_r^{(1)} \right\rangle$ in the simulation are shown by the blue and red solid lines, respectively. Here, the major radius $R_{\rm ax}$ is set to 12 m and the PS flow velocity $V_{Z,\parallel}^{\rm PS}$ is substituted into $V_{Z,\parallel}$ in the evaluation of the field-particle collision term $C_{\rm F}^{Zi} f_{{\rm M},Z}$.

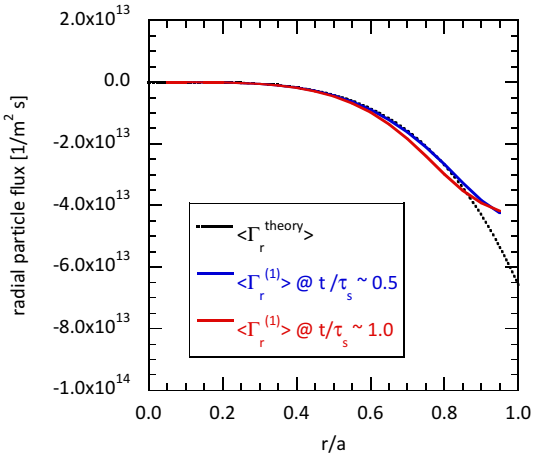

Figure 2. The radial particle fluxes $\left\langle \Gamma_r^{(1)} \right\rangle$ in the simulation at $t/\tau_{\rm s} \sim 0.5$ and 1.0 are shown by the blue and red solid lines, respectively. The theoretical estimate of the radial particle flux is illustrated by the black dashed line. Here, the major radius $R_{\rm ax}$ is set to 3 m.

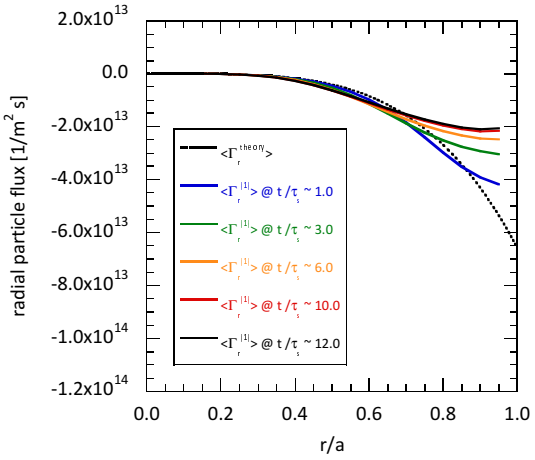

Figure 3. The relaxation of the radial particle flux $\left\langle \Gamma_r^{(1)} \right\rangle$ in the simulation is shown by the solid lines. In this case, δf_Z relaxes sufficiently after $t/\tau_\mathrm{s} \approx 10$. The theoretical estimate of the radial particle flux is illustrated by the black dashed line. Here, the major radius R_ax is set to 3 m.

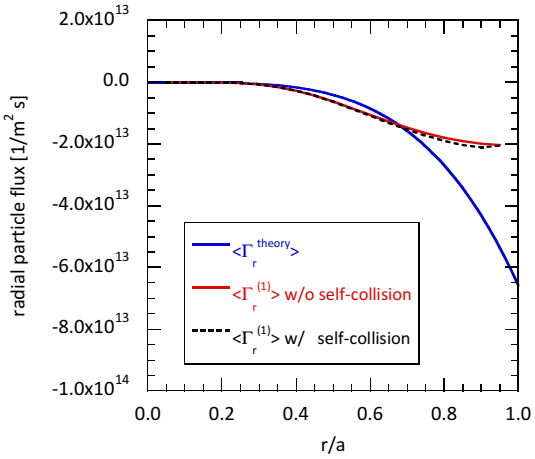

Figure 4. The radial particle fluxes $\left\langle \Gamma_r^{(1)} \right\rangle$ in the simulation with and without the self-collision term are shown by the black dashed line and the red solid line, respectively. The theoretical estimate of the radial particle flux is illustrated by the blue solid line. Here, the major radius R_ax is set to 3 m.

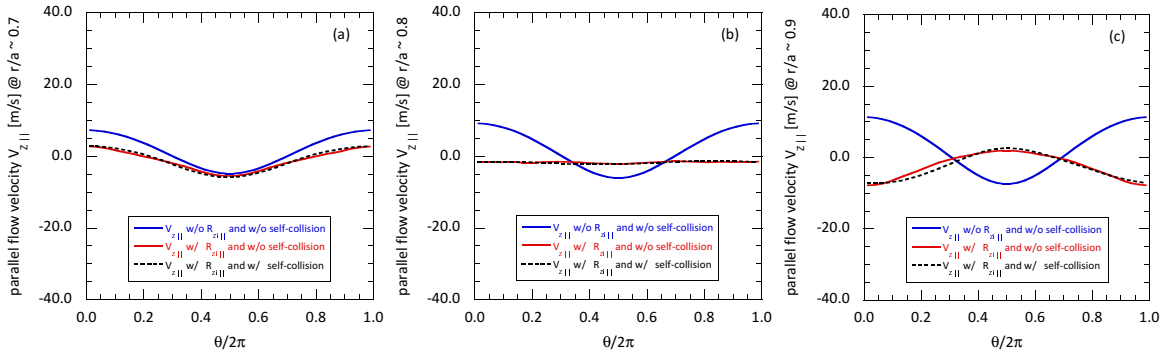

Figure 5. The parallel flow velocities $V_{Z,\parallel}$ of the impurity at $r/a \approx 0.7, 0.8$, and 0.9 in the simulations for the case of figure 4 are illustrated in figures (a), (b), and (c). Here, the parallel flow velocities in the simulations with and without the self-collision term are shown by the black dashed lines and the red solid lines, respectively. The velocity $V_{Z,\parallel}$ in the simulation in the case that all the Coulomb collision terms are ignored is given by the blue solid lines. In this case, the relation that $V_{Z,\parallel} - \langle V_{Z,\parallel} \rangle = V_{Z,\parallel}^{\rm PS}$ is satisfied. Note that the PS flow velocity of the background ion is $V_{i,\parallel}^{\rm PS} \approx -75.7 \cos\theta$ m/s at $r/a \approx 0.8$.

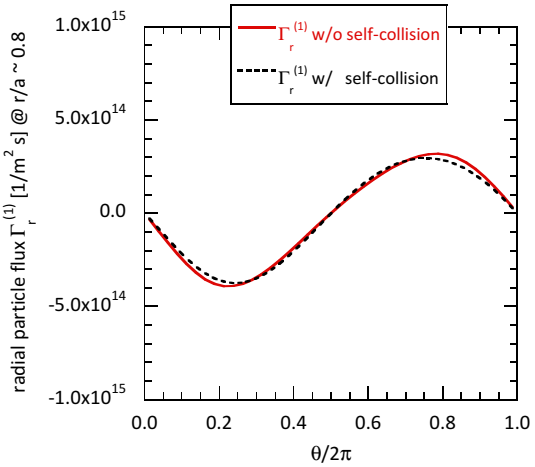

Figure 6. The poloidal dependence of the radial particle flux $\Gamma_r^{(1)} = \int {\rm d}^3 v \, (\mathbf{v} \cdot \nabla r) \, \delta f_Z$ at $r/a \approx 0.8$ in the simulation is illustrated for the case of figure 4. Here, the poloidal angle is given by θ. The results of the simulations with and without the self-collision term are shown by the black dashed line and the red solid line, respectively.

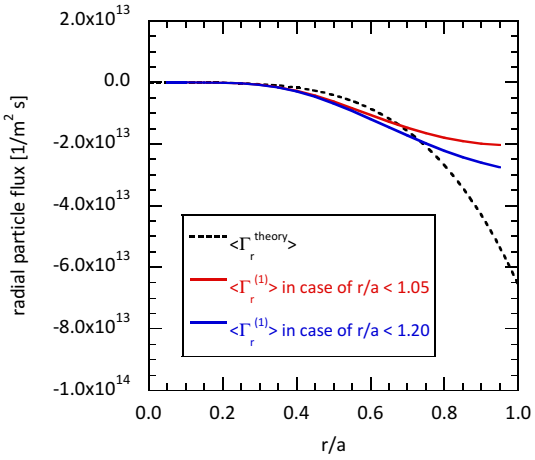

Figure 7. When the marker particles are distributed initially and uniformly in the region of $r/a < 1.20$, the radial particle flux $\left\langle \Gamma_r^{(1)} \right\rangle$ is shown by the blue solid line. On the other hand, the flux $\left\langle \Gamma_r^{(1)} \right\rangle$ for the case in which the marker particles are distributed initially and uniformly in the region of $r/a < 1.05$ is shown by the red solid line. The self-collision term is ignored in all the simulations in this figure. The theoretical estimate of the radial particle flux is illustrated by the black dashed line. The major radius $R_{\rm ax}$ is set to 3 m.

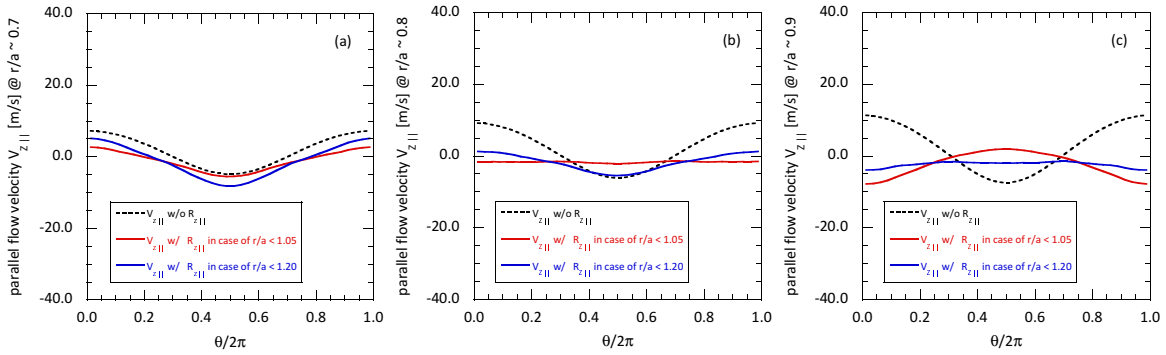

Figure 8. The parallel flow velocities $V_{Z,\parallel}$ of the impurity at $r/a \approx 0.7, 0.8$, and 0.9 in the simulations in figure 7 are illustrated in figures (a), (b), and (c). Here, the parallel flow velocities in the simulation with the marker particles distributed initially and uniformly in the region of $r/a < 1.20$ are shown by the blue solid lines. On the other hand, the parallel flow velocities in the simulation with the marker particles distributed initially and uniformly in the region of $r/a < 1.05$ are shown by the red solid lines. The parallel flow velocities in the case of ignoring the friction and the thermal forces are illustrated by the black dashed lines, which are independent from the simulation conditions in the region of $r/a > 1$. In this case, the relation that $V_{Z,\parallel} - \left\langle V_{Z,\parallel} \right\rangle = V_{Z,\parallel}^{\rm PS}$ is satisfied.

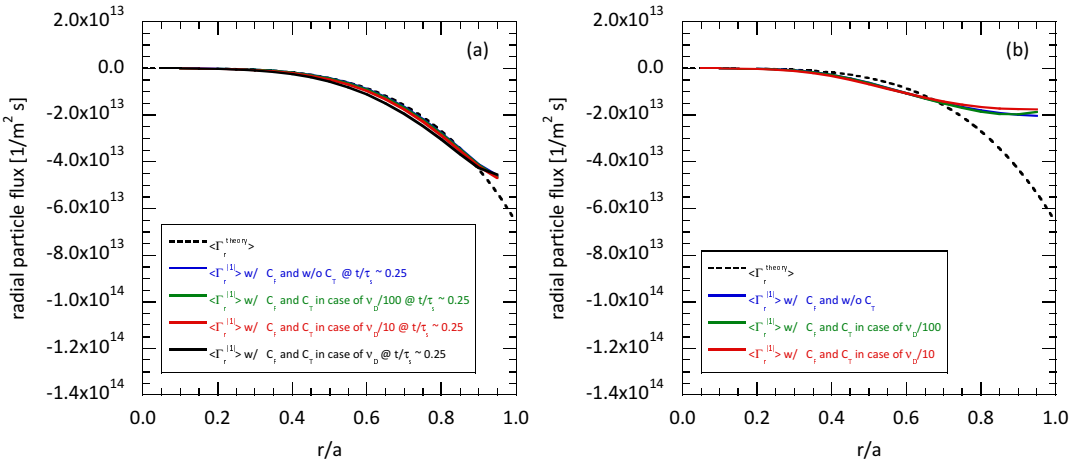

Figure 9. The radial particle fluxes $\left\langle \Gamma_r^{(1)} \right\rangle$ in the simulations with the test-particle collision term $C_{\rm T}^{Zi}\delta f_Z$ for the cases of $(\nu_{\rm D}^{Zi}/100)\mathscr{L}(\delta f_Z)$, $(\nu_{\rm D}^{Zi}/10)\mathscr{L}(\delta f_Z)$, and $\nu_{\rm D}^{Zi}\mathscr{L}(\delta f_Z)$ are shown by the green, red, and black solid lines, respectively. The flux $\left\langle \Gamma_r^{(1)} \right\rangle$ in the simulation without $C_{\rm T}^{Zi}\delta f_Z$ is illustrated by the blue solid lines. The self-collision term is ignored in all the simulations in these figures. The theoretical estimate of the radial particle flux is illustrated by the black dashed lines. (a) The simulation results at $t/\tau_{\rm s} \sim 0.25$ and (b) the results in the sufficiently relaxed states. Here, the marker particles are distributed initially and uniformly in the region of $r/a < 1.05$. The major radius $R_{\rm ax}$ is set to 3 m.

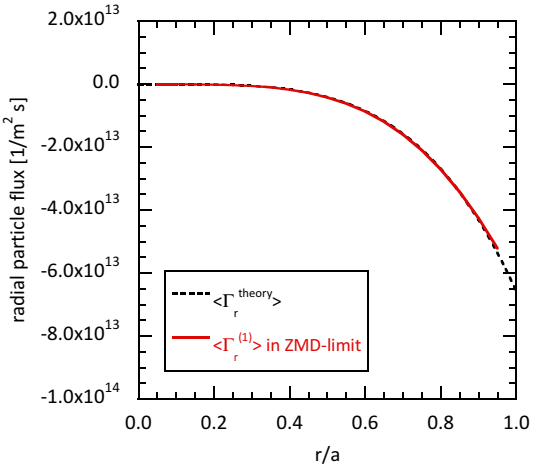

Figure A1. The radial particle flux $\left\langle \Gamma_r^{(1)} \right\rangle$ in the ZMD limit is shown by the red solid line. The theoretical estimate of the radial particle flux is illustrated by the black dashed line. Here, the major radius $R_{\rm ax}$ is set to 12 m.

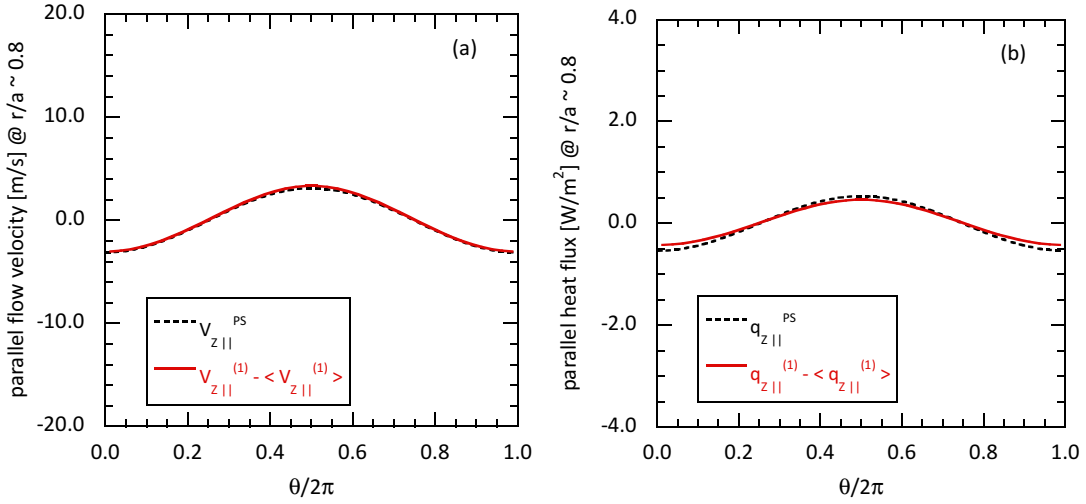

Figure A2. (a) The parallel flow velocity $V_{Z,\parallel}^{(1)} - \left\langle V_{Z,\parallel}^{(1)} \right\rangle$ evaluated at $r/a \approx 0.8$ in the simulation based on (19) is illustrated by the red solid line. The PS flow velocity $V_{Z,\parallel}^{\mathrm{PS}} \approx (2q/Ze n_Z B)\,(\mathrm{d}p_Z/\mathrm{d}r)\,\cos\theta$ is shown by the black dashed line. (b) The parallel heat flux $q_{Z,\parallel}^{(1)} - \left\langle q_{Z,\parallel}^{(1)} \right\rangle$ evaluated at $r/a \approx 0.8$ in the simulation based on (19) is illustrated by the red solid line. The PS heat flux $q_{Z,\parallel}^{\mathrm{PS}} \approx (5qn_Z T_Z/ZeB)\,(\mathrm{d}T_Z/\mathrm{d}r)\,\cos\theta$ is shown by the black dashed line. Here, the terms of the friction and the thermal forces and the self-collision terms are ignored in these figures. The major radius R_{ax} is set to 12 m.

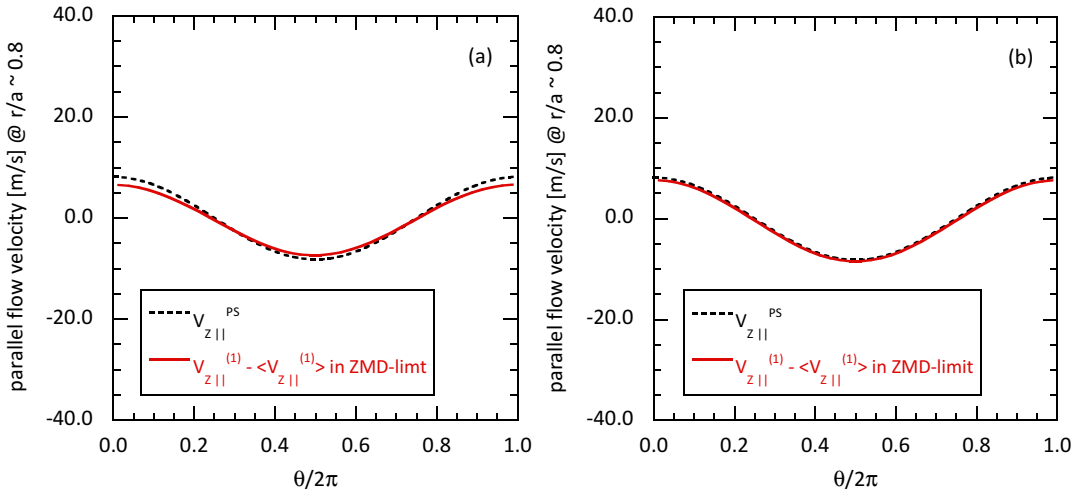

Figure A3. (a) The parallel flow velocity $V_{Z,\parallel}^{(1)} - \left\langle V_{Z,\parallel}^{(1)} \right\rangle$ evaluated at $r/a \approx 0.8$ by using KEATS code based on the local model in the case of considering $C_{\mathrm{F}}^{Zi}p$ is illustrated by the red solid line. This parallel flow velocity is calculated in the case of figure A1. (b) The parallel flow velocity $V_{Z,\parallel}^{(1)} - \left\langle V_{Z,\parallel}^{(1)} \right\rangle$ evaluated at $r/a \approx 0.8$ by using KEATS code based on the local model in the case of ignoring $C_{\mathrm{F}}^{Zi}p$ is illustrated by the red solid line. Here, the local model in these figures is described by equations (A2) and (A3). The PS flow velocity $V_{Z,\parallel}^{\mathrm{PS}}$ is shown by the black dashed lines. The major radius R_{ax} is set to 12 m.

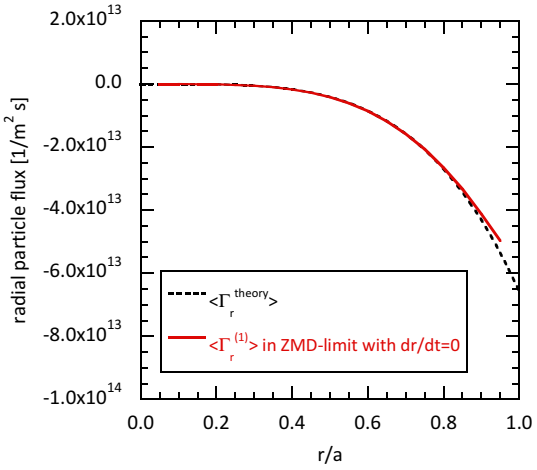

Figure A4. The radial particle flux $\left\langle \Gamma_r^{(1)} \right\rangle$ in the ZMD limit with $\dot{r} = 0$ is shown by the red solid line. The theoretical estimate of the radial particle flux is illustrated by the black dashed line. Here, the major radius $R_{\rm ax}$ is set to 12 m.

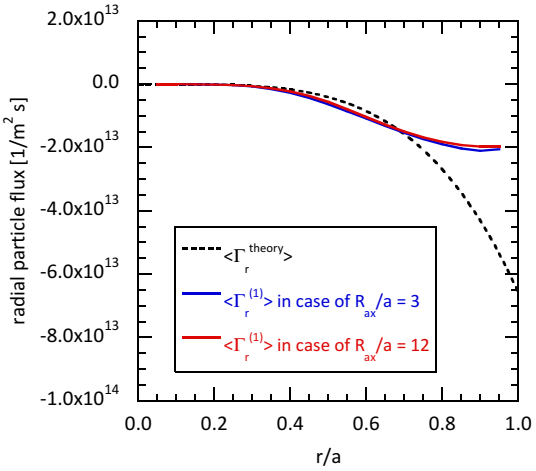

Figure A5. In the case of $R_{\rm ax}/a = 12$, the radial particle flux $\left\langle \Gamma_r^{(1)} \right\rangle$ evaluated by using KEATS code based on the global model is shown by the red solid line. In the case of $R_{\rm ax}/a = 3$, the flux $\left\langle \Gamma_r^{(1)} \right\rangle$ evaluated by using KEATS code based on the global model, which is shown in figure 4, is illustrated by the blue solid line. The theoretical estimate of the radial particle flux is shown by the black dashed line.